Effects of Torsional Stiffness and Inertia on a Passively Deployable Flap for Aerodynamic Lift Enhancement

Nirmal J. Nair* and Andres Goza[†] *University of Illinois at Urbana-Champaign, Urbana, Illinois, 61801*

Birds can perform low-speed maneuvers at post-stall angles of attack (AoAs), owing in part to covert feathers—a set of self-actuating feathers located on the upper surface of the wings. During unsteady flow separation at large AoAs, these feathers protrude into the flow and provide lift enhancements, for reasons that are still not fully understood. To facilitate the use of covertfeather-inspired designs in bio-inspired aerial vehicles, and to enable plausible hypotheses for the utility of these feathers in biological flight, we investigate a model system in which a passively deployable, torsionally hinged flap is mounted on the suction surface of a stationary airfoil at a Reynolds number of Re = 1,000. We perform high-fidelity nonlinear simulations to quantify the effect of flap moment of inertia, torsional stiffness, and chordwise location on aerodynamic performance. We identify parameter values that provide lift improvements as high as 27% relative to the baseline flap-less case. Torsional stiffness is found to dictate the mean deflection angle of the flap, and the rotational inertia is demonstrated to determine the time dependent dynamics about that position. Behavioral regimes that categorize the dynamics of the flow-airfoil-flap system are provided using a k-means clustering algorithm from two meaningfully chosen length scales. The dominant physical mechanisms responsible for delivering significant aerodynamic benefits characteristic to these regimes are identified and a qualitative comparison between these regimes is performed.

I. Nomenclature

angle of attack α flap deployment angle $\overline{\beta}$ mean flap deployment angle airfoil chord length C_l coefficient of lift = coefficient of pressure percentage change in mean lift relative to baseline airfoil surface stress on body integrated force on the airfoil in y-direction set of bodies Γ_a, Γ_f bodies of airfoil and flap dimensionless and dimensional flap moment of inertia i_{β}, I_{β} k_{β}, K_{β} dimensionless and dimensional stiffness of torsional spring dimensionless and dimensional chordwise flap location l_{β}, L_{β} kinematic viscosity dimensionless and dimensional pressure field p, Pfreestream pressure P_{∞} fluid density ρ_f = Re= Reynolds number time period of steady limit cycle oscillations (LCO) fluid velocity u

^{*}Graduate Research Assistant, Department of Aerospace Engineering.

[†]Assistant Professor, Department of Aerospace Engineering.

 U_{∞} = freestream velocity

 χ, χ_a, χ_f = Lagrangian coordinate of body, airfoil and flap

 χ_f^0 = flap hinge location Ω = flow domain

II. Introduction

Birds have a remarkable ability to fly under adverse conditions of sudden gusts and successfully perform high angles of attack maneuvers during landing and take-off. They possess a biological flow control device in the form of covert feathers to aid such maneuvers [1, 2]. Covert feathers are a set of self-actuating feathers located on the upper surface of the wings. During unsteady flow separation at large angles of attack, these feathers passively deploy into the flow and augment the lift. The physical mechanisms by which they enhance flight performance can be exploited in designing bio-inspired micro and unmanned aerial vehicles with high agility and maneuverability [3–5]. Understanding the flow physics of this passive flow control technique is still an active area of research.

Several experimental and numerical studies have modeled covert feathers as a rigidly attached or freely moving flap on the upper surface of a wing. These studies have reported significant improvements in lift [6, 7] at large angles of attack. Such lift enhancements are also found to delay stall and reduce the drop in lift post-stall [8, 9]. The improvement in lift was associated to a "pressure dam" effect [10] where the flap mitigates the propagation of the rearward pressure upstream and thereby maintains a low pressure region upstream of the flap. Other factors for lift improvement included a delayed flow separation location and preventing reversed flow from advancing upstream towards the leading edge[11]. More recently, a leading edge vortex induced by the alula, a type of covert feather, was found to enhance lift when maneuvering at low speeds [12]. Besides lift enhancements, these flaps have also been found to reduce fluctuations in lift and drag due to vortex shedding [13].

A more realistic model for covert feathers involves mounting the flap on the wing via a torsional spring. This setup could avoid the occurrence of a free (zero-stiffness) flap over-deploying onto the suction surface in the presence of significant flow separation [11], and eliminate the need for active actuation that would be required with static flaps (and most other actuation approaches). Furthermore, the torsional stiffness of the spring and rotational inertia of the flap can be used as additional tunable parameters to further augment the lift of freely moving flaps [14]. However, a comprehensive study of the flow physics of a passively deployable, torsionally attached flap on an airfoil and it's potential for lift enhancement has not been done in literature.

In this work, we perform nonlinear, two-dimensional (2D) high-fidelity simulations of flow past an airfoil with a passively deployable, torsionally mounted flap on the upper surface of a stationary airfoil. These fluid-structure interaction (FSI) simulations are strongly-coupled allowing for a wide range of moment of inertia of the flap and stiffness of the spring varying over several orders of magnitude to be considered. The Reynolds number of the flow based on the chord length is set to 1,000 and the angle of attack is fixed at 20° . A systematic parametric study is performed by varying the flap hinge location, rotational inertia and torsional stiffness to identify parametric regions that provide significant lift benefits. A flow classification methodology based on meaningfully chosen length scales of the FSI system is then performed to categorize all the parametric cases into different flow regimes. The key flow structures of the lift enhancing flow regimes are then analyzed and qualitatively compared.

The remainder of the manuscript is organized as follows. In Sec. III, we describe the problem setup of a passively deployable torsional flap on an airfoil and the numerical method used to simulate the flow problem. In Sec. IV, we discuss the results of the parametric study, classification algorithm and flow physics of the lift enhancing regimes. Finally, conclusions are offered in Sec. V.

III. Problem setup and numerical methodology

A. Problem setup

In this work, we consider a stationary NACA0012 airfoil of chord length c at an angle of attack of $\alpha = 20^{\circ}$ in a flow with freestream velocity U_{∞} . The Reynolds number based on the chord length is set to Re = 1,000. A flap of length 0.2c is hinged on the upper surface of the airfoil via a torsional spring, as shown in Fig. 1, where the instantaneous deployment angle of the flap is given by β . The parameters that govern the dynamics of the airfoil-flap system are the dimensionless moment of inertia of the flap, i_{β} , stiffness of the torsional spring, k_{β} , chordwise distance of the flap from

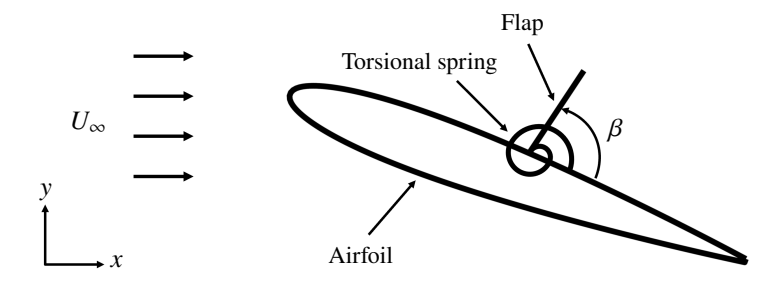


Fig. 1 Schematic of the system of passively deployable flap on an airfoil

the leading edge, l_{β} , and Reynolds number defined as,

$$i_{\beta} = \frac{I_{\beta}}{\rho_f c^4}, \qquad k_{\beta} = \frac{K_{\beta}}{\rho_f U_{\infty}^2 c^2}, \qquad l_{\beta} = \frac{L_{\beta}}{c}, \qquad Re = \frac{U_{\infty} c}{v}.$$
 (1)

Here, I_{β} , K_{β} and L_{β} are the dimensional counterparts of i_{β} , k_{β} and l_{β} ; and ρ_f and ν are the density and kinematic viscosity of the fluid. The parameter l_{β} is reported as percentage of chord length from the leading edge in this manuscript. Initially, the flap is rested at an angle of 5° from the airfoil surface, which is taken as the undeformed (zero stress) deflection angle. As the vortex shedding process occurs at the high angle of attack of 20°, the flap passively deploys and interacts with the flow.

The aerodynamic performance of the airfoil-flap system will be often analyzed in terms of coefficients of lift and pressure defined as,

$$C_l = \frac{F_y}{\frac{1}{2}\rho_f U_{\infty}^2 c}, \qquad C_p = \frac{P - P_{\infty}}{\frac{1}{2}\rho_f U_{\infty}^2},$$
 (2)

where F_y is the dimensional integrated force along the baseline airfoil (not including the flap) in the y direction, P is the dimensional pressure variable and P_{∞} is the freestream pressure.

B. Numerical methodology

The simulations are performed using the strongly-coupled immersed boundary method of Goza and Colonius [15] which has been implemented and verified on problems involving torsionally mounted flaps [16]. This method solves the following dimensionless governing equations,

$$\frac{\partial \mathbf{u}}{\partial t} + \mathbf{u} \cdot \nabla \mathbf{u} = -\nabla p + \frac{1}{Re} \nabla^2 \mathbf{u} + \int_{\Gamma} f(\chi(s, t)) \delta(\chi(s, t) - \mathbf{x}) ds$$
 (3)

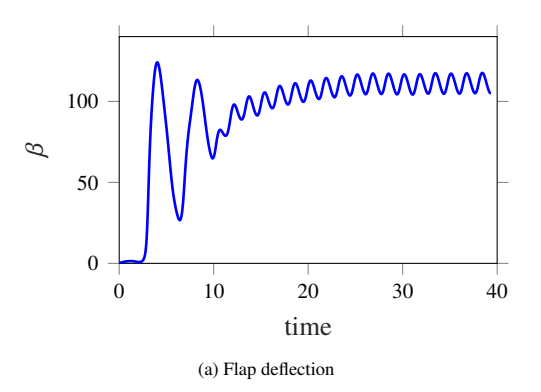
$$\nabla \cdot \boldsymbol{u} = 0 \tag{4}$$

$$i_{\beta} \frac{\partial^{2} \beta}{\partial t^{2}} + k_{\beta} \beta = -\int_{\Gamma_{f}} (\chi_{f} - \chi_{f}^{0}) \times f(\chi_{f}) d\chi_{f}$$
 (5)

$$\int_{\Omega} u(x)\delta(x - \chi_a)dx = 0$$
 (6)

$$\int_{\Omega} u(x)\delta(x - \chi_f)dx = \frac{\partial \beta}{\partial t}\hat{e}^i \times (\chi_f - \chi_f^0)$$
 (7)

In the above, x denotes the Eulerian coordinate representing a position in the fluid domain Ω and $\chi(s,t)$ denotes the Lagrangian coordinate attached to the bodies (airfoil and flap) in the set Γ , the surface of which is parametrized by the variable s. These variables, x, χ and s were nondimensionalized by c; velocity u was nondimensionalized by U_∞ ; time t was nondimensionalized by c/U_∞ ; pressure p and surface stress imposed on the fluid by the body f were nondimensionalized by $\rho_f U_\infty^2$, where ρ_f is the fluid density. The equation of motion of the torsional flap Γ_f is given by Eq. (5) where χ_f is the Lagrangian coordinate of Γ_f . The term on the right hand side of Eq. (5) represents the



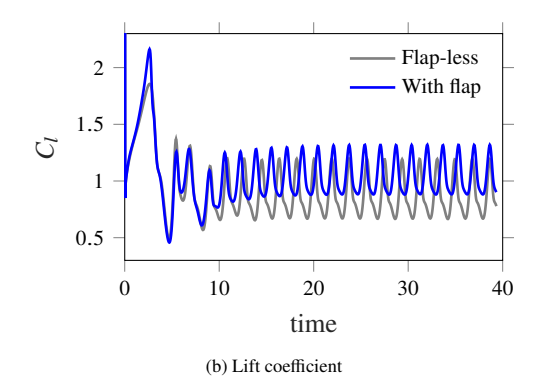


Fig. 2 Plots of flap deflection, β , and lift coefficient, C_l , for the flap-less case and the case of flap hinge located at 50% of the chord length from the leading edge, $k_{\beta} = 0.0015$ and $i_{\beta} = 0.001$.

moment about χ_f^0 due to the surface stress imposed on the fluid by the flap (thereby resulting in a negative sign). The no-slip boundary constraints on the airfoil and flap are given by Eq. (6) and (7), respectively. Here, \hat{e}^i is a unit vector denoting the direction of the angular velocity of the flap and χ_a is the Lagrangian coordinate of the airfoil. These no-slip constraints are used to solve for the surface stress term $f(\chi)$ that enforces the boundary condition that must hold on the respective bodies.

The flow equations (3)–(4) are spatially discretized using the standard second-order finite difference method and rewritten in a streamfunction-vorticity formulation. For time-discretization, Eq. (3) utilizes an Adams-Bashforth scheme for the nonlinear term and a Crank-Nicolson method for the diffusive term. The equation of motion of the flap (5) is discretized using an implicit Newmark scheme. The boundary condition constraints (6)–(7) and the surface stress term in Eq. (3) are evaluated implicitly at the current time step to enable stability of the method for flaps with a wide range of inertia and stiffness. The resulting fully discretized system of equations are subjected to a block-LU decomposition and iterated using Newton's method until convergence for the flap deflection angle. A multi-domain approach for far-field Dirichlet boundary conditions of zero vorticity is incorporated for solving the flow equations where a hierarchy of grids of increasing coarseness stretching to the far field is employed (see reference [17] for details).

A grid-convergence study for the passively deployable airfoil-flap system was performed in Nair and Goza [16]. The converged spatial grid and time step sizes are set to be $\Delta x/c = 0.00349$ and $\Delta t/(c/U_{\infty}) = 0.0004375$, respectively. Following Goza and Colonius [15], the immersed boundary spacing is set to be twice as that of the flow grid spacing of the finest grid. The convergence criteria for the fluid-structure coupling equation (not shown here; see reference [16]) is $\|\Delta\beta\|_{\infty} \le 10^{-7}$. For the multi-domain approach for far-field boundary conditions, five grids of increasing coarseness are used where the finest and coarsest grid levels are $[-0.5, 2.5]c \times [-1.5, 1.5]c$ and $[-23, 25]c \times [-24, 24]c$, respectively.

IV. Results

A. Qualitative flow features

We begin with an overview of the flow features for a representative case of the flap hinged at 60% of the chord length from the leading edge, $k_{\beta}=0.0015$ and $i_{\beta}=0.001$. The flow-field at the angle of attack of $\alpha=20^{\circ}$ is unsteady due to a periodic vortex shedding process, which is present even in the baseline case without a flap and is modulated by the flap dynamics. This unsteady nature is manifested in the temporal plots of the sectional lift, C_l , and the torsional flap motion, β , in Fig. 2. It can be observed from Fig. 2a that the flap initially begins from its undeformed configuration on the airfoil surface, $\beta=0^{\circ}$. During the initial transient period from t=0 to $t\approx 5$, a vortex is shed from the leading edge of the airfoil and advects downstream above the surface of the airfoil and flap. The low pressure of the advecting leading edge vortex (LEV) pulls the flap away from the airfoil, resulting in a large deflection of the flap at $t\approx 3$. The passively deployed flap then continues to respond to the aerodynamic forces generated by the alternate shedding of vortices from the leading and trailing edges. After a transient period from $t\approx 3$ to $t\approx 20$, the airfoil-flap system enters periodic limit cycle oscillation (LCO) where the flap oscillates about a mean deflection angle, $\overline{\beta}$, while the amplitude of flap oscillations approximately remains constant. The lift response of the baseline airfoil in the airfoil-flap system (c.f. Fig. 2b) also exhibits similar LCO behavior after an initial transient. In this work, we focus on the flow physics in the

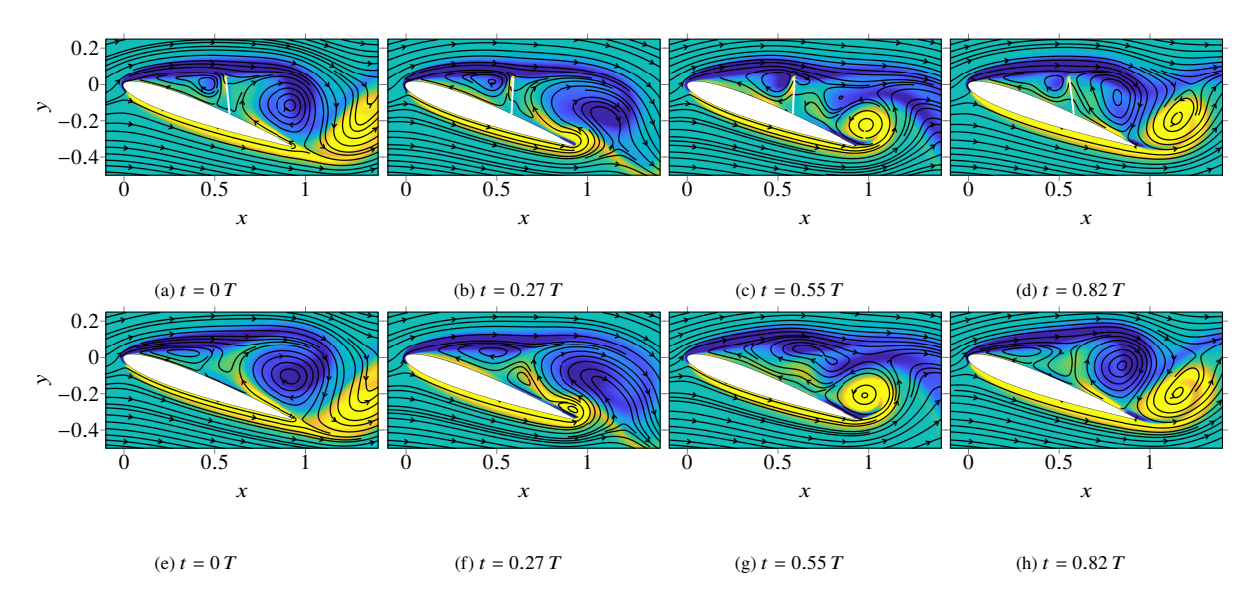


Fig. 3 Vorticity contours at different time instants in one period of lift cycle for the case of flap hinge located at 60% of the chord length from the leading edge, $k_{\beta} = 0.0015$ and $i_{\beta} = 0.001$ (first row) and the flap-less baseline case (second row).

LCO regime, t > 20, after the decay of any transients.

Vorticity snapshots at four time instants over one lift cycle in the steady LCO regime are shown in Fig. 3a–3d,where one lift cycle is defined between two consecutive peaks of C_l . The periodic formation, shedding and interaction of the vortices from the leading and trailing edges can be clearly observed from these plots. At t/T = 0, the fully rolled up LEV from the previous cycle resides above the trailing edge as shown in Fig. 3a and provides maximum lift. As the LEV continues to advect downstream, a trailing edge vortex (TEV) begins to form at $t/T \approx 0.27$ and continues to roll up at $t/T \approx 0.55$ as shown in Fig. 3c. The growing strength of the TEV reduces the clockwise circulation around the airfoil, decreases the pressure on the lower surface, and thereby reduces the lift. As the TEV advects downstream, a newly formed LEV continues to grow and advect, gaining in circulation strength as shown in Fig. 3d. Eventually, the rolled-up LEV reaches the trailing edge and the cycle is repeated.

Similar vortex shedding phenomena is also observed in the case of an airfoil without a flap as depicted in Fig. 3e–3h. The corresponding lift response for this flap-less case is plotted in Fig. 2b. Although the lift response of the flap and flap-less cases are qualitatively similar, the former provides a mean lift improvement of $\Delta \overline{C}_l \approx 20\%$ relative to the flap-less case. In what follows, we present results from a systematic parametric study of the flow-flap-airfoil system dynamics for a range of stiffness, k_{β} , and torsional inertia, i_{β} , values. We characterize the qualitatively distinct regimes that the fully coupled FSI system exhibits, and provide insights into the interplay between the flap dynamics and the formation and interaction of vortical structures for parameters yielding lift benefits.

B. Parametric study

A parametric study is performed to characterize the effect of various parameters on aerodynamic processes and identify regions of parametric space beneficial for lift performance. The varying parameters in this study are stiffness, inertia and location of the hinge. Inertia is varied as $i_{\beta} \in \{10^{-5}, 10^{-4}, 10^{-3}, 10^{-2}\}$ while stiffness is varied as $k_{\beta} \in [10^{-4}, 10^{-1}]$. Two flap locations of 50% and 60% of the chord length from the leading edge are considered. For every flow simulation, the mean lift of the airfoil in the steady LCO regime (t > 20) is computed and the improvement with respect to the mean lift of the flap-less case is reported.

The results of the parametric study for the cases of 50% and 60% hinge locations are plotted in Fig. 4a and 4b, respectively. In each plot, $\Delta \overline{C}_l$ in percentage is plotted against k_β for various i_β . The passively deployable flap is able to deliver lift benefits as high as 17% and 27% greater than the flap-less system for the 50% and 60% hinge cases, respectively. To systematically characterize the effects of different parameters, we first discuss the variations in performance trends due to hinge location. For both the 50% and 60% cases, certain ranges of stiffness are observed to provide maximum lift benefits. For the 50% flap location, optimal lift is achieved around $k_\beta \approx 0.0015$ for all values of

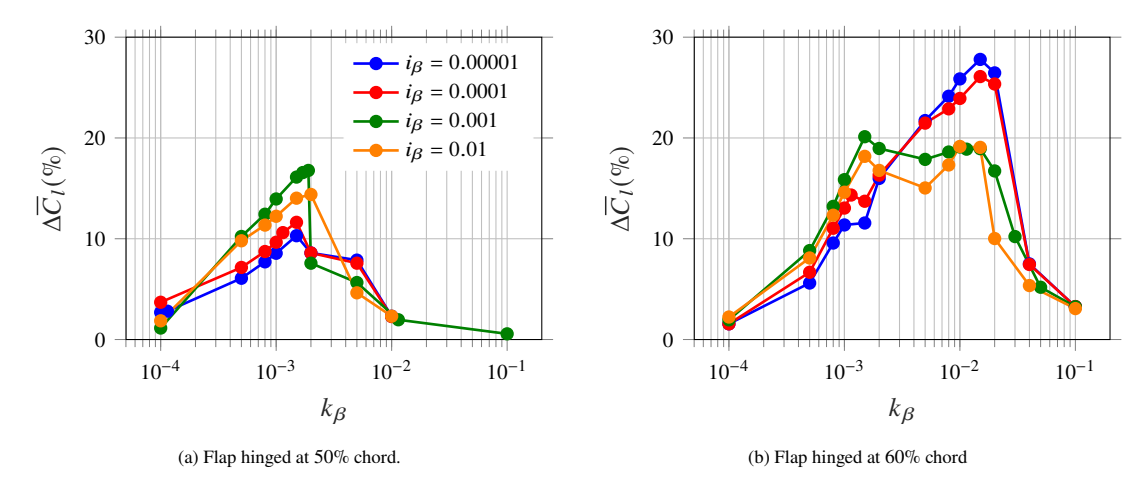


Fig. 4 Performance plots of percentage change in mean lift for various cases of inertia, stiffness and hinge location.



Fig. 5 Mean flap configurations for the case of 60% hinge location and $i_{\beta} = 0.001$.

inertia. In contrast, for the 60% case, a large peak is observed at $k_{\beta} \approx 0.01$ for all cases of inertia. However, for large values of inertia, an additional peak is observed at $k_{\beta} \approx 0.0015$. The fact that both 50% and 60% cases provide enhanced lift at similar stiffness of $k_{\beta} \approx 0.0015$ for a considerable variation in inertia indicates that the this peak corresponds to a flow regime that exhibits similar physical characteristics. In contrast, the peak at $k_{\beta} \approx 0.01$ for the 60% case potentially belongs to a different physical regime. Further discussion about these two postulated regimes can be found in Sec. IV.C.

One of the dominant effects of stiffness is to set a nominal mean deflection angle about which the flap oscillates. To demonstrate this fact, airfoil-flap configurations with the flap illustrated at its mean deflection angle are shown in Fig. 5 for four different stiffness values for the 60% hinge location and $i_{\beta}=0.001$. Though not pictured, we note that similar mean deployment angles occur at the captioned stiffness values for the other inertia values and hinge location. This independence of inertia suggests that the mean flap location is largely set by a balance between the internal hinge strains at the mean flap location and the mean flow forces, and are (largely) agnostic to the time-dependent flap dynamics. This will be discussed in the final manuscript. Fig. 5a demonstrates that for a very low stiffness of $k_{\beta}=10^{-4}$, the restoring torque of the torsional spring is significantly smaller than the aerodynamic forces of vortex shedding, resulting in the flap flipping forward (upstream). As the stiffness is increased, the mean deflection decreases as shown in Fig. 5b and 5c due to increased restoring torque. For very large stiffness of $k_{\beta}=0.05$, the flap hardly deploys (c.f. Fig. 5d), since the restoring torque dominates over moments due to aerodynamic forces. Since the stiffness and mean deflection angle are strongly correlated, we re-plot the performance plots from Fig. 4 but now with $\overline{\beta}$ along the x-axis in Fig. 6. It can be clearly seen that the cases corresponding to extreme flap configurations of Fig. 5a and 5d do not provide considerable performance benefits regardless of inertia. Therefore, stiffness is a crucial parameter in setting a mean flap configuration that is capable of generating significant lift.

We now discuss the effect of inertia on lift performance. We note from Fig. 6 that across four orders of magnitude of inertia, the general trend in the mean lift improvement of the moving flap follows the trend of a rigid flap. Here, the data for the rigid flap were obtained via rigid body simulations of the airfoil-flap system with a stationary rigid flap affixed at various deployment angles. Of course, for higher inertia values the trends become increasingly similar to the rigid case (indeed, one recovers the rigid flap scenario for $i_{\beta} \to \infty$). This qualitative similarity in trend suggests that (i) the mean deflection angle is set largely by the stiffness k_{β} , and (ii) this mean deflection angle is the primary parameter in setting the qualitative flow regime and associated aerodynamic performance. At the same time, there are detailed differences

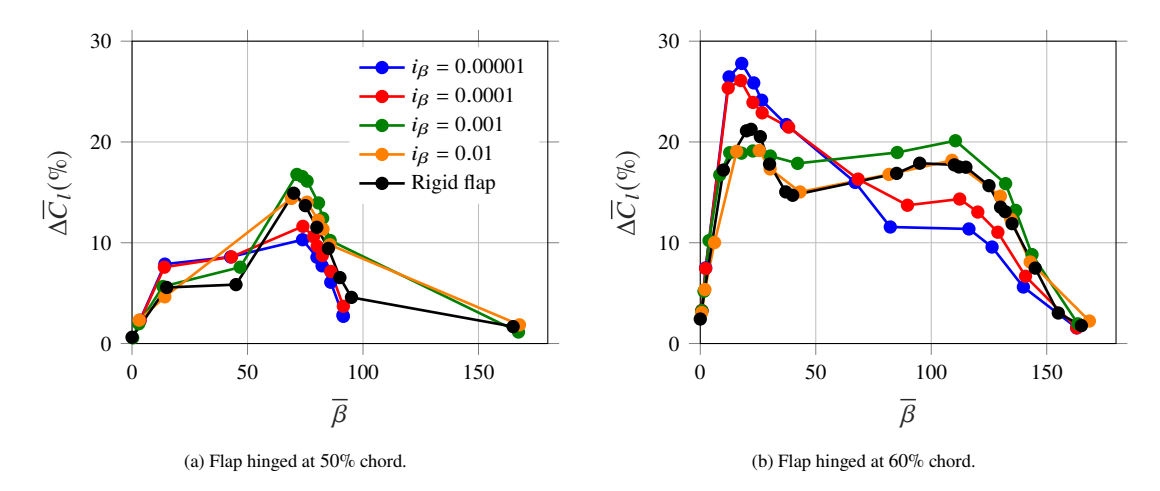


Fig. 6 Performance plots showing percentage change in mean lift for various cases of inertia, stiffness dependent mean flap deflection and hinge location.

across inertia values indicated in Fig. 6 that suggest that the time-dependent flap dynamics have a secondary effect in establishing the FSI dynamics and corresponding lift behavior.

We note that the effect of the time-dependent flap dynamics about the mean angle, encoded in the inertia i_{β} , is not uniformly beneficial or deleterious for performance. For example, we note from Fig. 6 that there are peaks across all inertia values near $\overline{\beta} \approx 65^{\circ}$ at 50% and $\overline{\beta} \approx 110^{\circ}$ at 60%. (These peaks both correspond to a stiffness value of $k_{\beta} \approx 0.0015$; as mentioned above, the appearance of a performance peak at the same stiffness value across multiple inertia values and over different flap locations suggests a common behavioral regime, as will be shown in Sec. IV.C below). For this set of peaks, the lighter flaps perform more poorly than the heavier (or even rigid) ones. By contrast, for the peak near $\overline{\beta} \approx 25^{\circ}$ at 60%—which will be shown in Sec. IV.C to correspond to a different behavioral regime—the lighter flags provide larger mean lift benefits. Thus, in the former (latter) regime modest (larger amplitude) flap dynamics about the mean deflection angle yield improvements to mean lift.

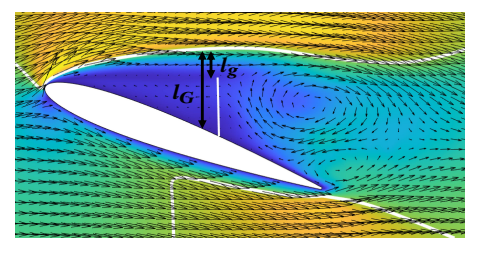
Altogether, these parametric studies suggest that the dominant parameter in setting the mean deflection angle and associated behavioral regime and mean lift characteristics is the stiffness k_{β} . The data also indicates that there is a secondary effect on the behavioral regime and performance that are encoded in the time-dependent dynamics of the flap about the mean deployment angle, which is dictated by the flap inertia i_{β} . In the next section, we use these observations to further characterize the different qualitative regimes of the FSI system and their effects on performance.

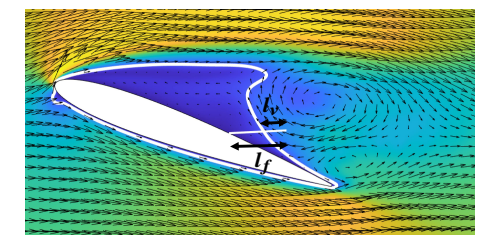
C. Classification of regimes

Noting the primary importance of the stiffness-dependent mean flap configurations, we center our analysis on time-averaged data. The mean velocity magnitude contour for the flap-less case is plotted in Fig. 7. The mean is evaluated using eleven snapshots of velocity magnitude uniformly collected in one time period of the lift cycle. We emphasize that the contour of the flap-less case is considered instead of the flap cases to identify the locations of the baseline flow-field modified by the flap. Now, on top of this contour, we superimpose the mean flap configurations corresponding to $k_{\beta} = 0.0015$ and $k_{\beta} = 0.01$ in Fig. 7a and 7b, respectively, with hinge location at 60% chord and $i_{\beta} = 0.001$.

For the case of $k_{\beta}=0.0015$ in Fig. 7a, the large flap deflection is such that the flap tip lies in close vicinity of the high momentum shear layer. For reference, the outer boundary of the shear layer is outlined by a white contour line which is defined similarly to a boundary layer as $|u|/U_{\infty}=0.99$. This contour line divides the separated flow region from the free-stream. We note that the vortex shedding process (visualized by the velocity vectors) occurs downstream of the flap. Because of the flap's proximity to the shear layer, we associate $k_{\beta}=0.0015$ with the flap-shear interaction regime.

For the case of $k_{\beta}=0.01$ in Fig. 7b, the mean flap configuration is such that a portion of the flap lies in the vortex shedding region. For reference, a white contour line corresponding to $|u|/U_{\infty}=0.25$ of the same mean baseline velocity flow-field is plotted. The value $|u|/U_{\infty}=0.25$ is chosen to approximately outline a recirculation zone that excludes the vortex shedding region. Since a portion of the flap lies within the vortex shedding zone, implying the potential for





(a) Gap ratio in flap-shear interaction regime

(b) Flap ratio in flap-vortex interaction regime

Fig. 7 Demonstration of length scales in the primary flow regimes. Both contour plots are identical and correspond to the mean velocity magnitude of the flap-less case.

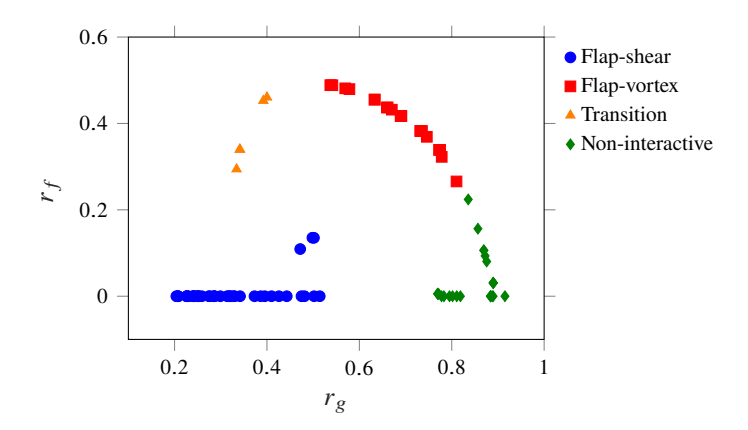


Fig. 8 Clusters determined by the k-means algorithm with gap ratio, r_g and flap ratio, r_f as the inputs. The data points include all the cases of inertia, stiffness and hinge location considered in the parametric study.

flap-vortex interactions, we associate $k_{\beta} = 0.01$ with the flap-vortex interaction regime.

Fig. 7 demonstrates that, as postulated, $k_{\beta} = 0.01$ and $k_{\beta} = 0.0015$ coincide with two different regimes. To classify the dynamics for remaining stiffness values and account for the secondary effects of inertia, we now define two length scales. Since the flap-shear interaction regime is characterized by small gap between the flap tip and shear layer, we ascribe the length scale for this regime to be the gap ratio, $r_g = l_g/l_G$. Here l_g is the distance between the flap tip and the nearest point on the shear layer while l_G is the vertical distance between the corresponding point on the shear layer and the airfoil surface. These dimensions are also sketched in Fig. 7a. On the other hand, since the flap-vortex interaction regime is characterized by increased interaction of the flap with vortex shedding, we ascribe the length scale for this regime to be the flap ratio, $r_f = l_v/l_f$. Here, l_v is the length of the portion of the flap inside the vortex region, while l_f is the total length of the flap. These dimensions are also sketched in Fig. 7b.

We use a k-means clustering algorithm to segregate the data using the gap ratio and flap ratio. The number of clusters is set to k = 4 and the algorithm is repeated 50 times on the same data-set to ensure global convergence. The resulting clusters determined by the algorithm are plotted in Fig. 8, which contains the data for all stiffness and inertia values as well as both flap locations. We first note the cases lying in the flap-shear and flap-vortex interaction regime. The flap-shear regime is characterized by a low gap ratio (the flap is near the shear layer) and flap ratios (the flap does not protrude into the vortex region). By contrast, the flap-vortex regime is characterized by a large gap ratio (the flap is far away from the nominal mean shear layer) and flap ratio (the flap is deflected downwards and into the region where it will interact with vortex-shedding phenomena). The third cluster corresponds to a transition regime between the primary two regimes (the large flap ratio indicates protrusion into the region where vortex shedding will occur but the small gap ratio suggests that the flap remains significantly deployed, so that the interaction dynamics with the vortex-shedding process are fundamentally distinct from those in the flap-vortex interaction regime). Finally, the last cluster corresponds to all the non-interactive cases—the mean lift is essentially unchanged from the baseline (flap-less) case because the flap is nearly entirely un-deployed (c.f., Fig. 5d) or the flap has completely flipped over (c.f., Fig. 5a).

Using these clustering results, the performance plots in Fig. 4 are re-framed as performance maps as shown in

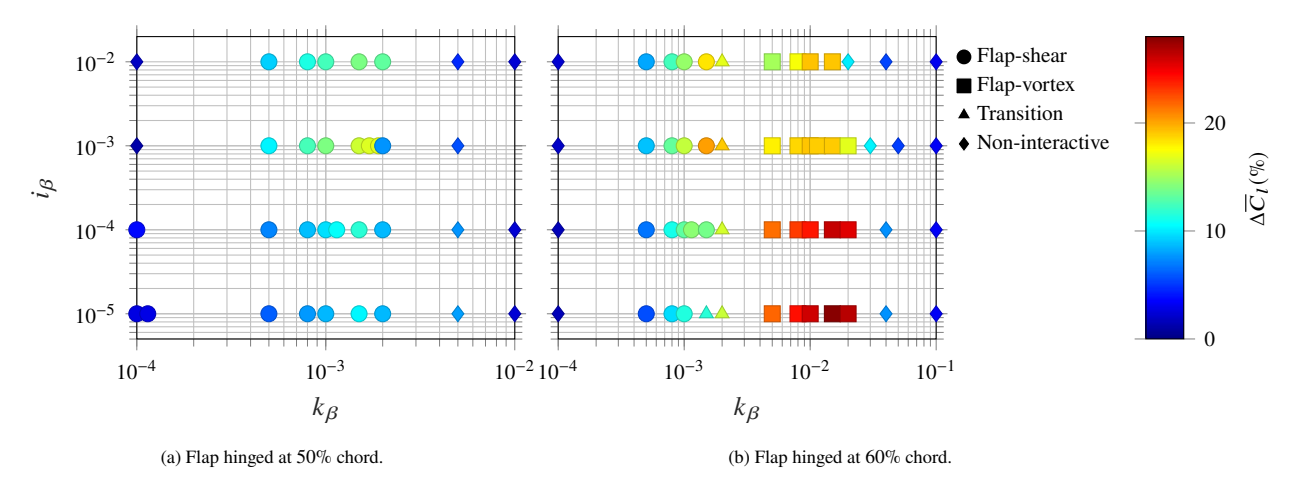


Fig. 9 Performance maps showing percentage change in mean lift for various cases of inertia, stiffness and hinge location. Parametric cases belonging to the same flow regime are assigned the same markers.

Fig. 9. Parametric cases belonging to the same regime are assigned the same markers. As expected, the cases with k_{β} in the vicinity of $k_{\beta} = 0.0015$ belong to the flap-shear interaction regime for both 50% and 60% cases. This also includes cases with lowest inertia at 60% location which did not have a distinct second peak in Fig. 4b. Similarly, the cases around $k_{\beta} = 0.01$ are assigned to the flap-vortex interaction regime in the 60% case. Note that none of the cases at the 50% location fall under the flap-vortex regime. This is because, for a fixed flap length of 0.2c, the flap is unable to interact with the vortices when the flap is located relatively upstream at 50% chord. We also observe that the cases near the local minima of Fig. 4b are assigned to the transition regime. Finally, cases at the extreme ends of the parameter space are grouped together into the non-interactive regime since they hardly interact with either the shear layer or vortices and therefore do not provide considerable improvement in lift in comparison to the interactive regimes.

The combined results of the parametric study and flow classification indicate that stiffness is a more dominant parameter in setting the flow regimes. Therefore, in this manuscript, we only explore the effect of stiffness-determined mean flap deflection on aerodynamic performance. Specifically, in the following sections, we describe the dominant physical mechanisms that yield high lift in the flap-shear and flap-vortex interaction regimes.

D. Flap-shear interaction regime

We motivate the driving physics in this regime with a representative case of the flap fixed at 50% location, $k_{\beta} = 0.0015$ and $i_{\beta} = 0.001$ and plot C_p on the airfoil surface and corresponding vorticity contours at four time instants in one time period in Fig. 10a–10d and Fig. 10e–10h, respectively. A step discontinuity in C_p on the suction surface of the airfoil at the location of the hinge is observed in each plot. This discontinuity is attributed to the "pressure dam" effect, also identified in Bramesfeld and Maughmer [10] and described as follows. At large flap deployment angles, the flap acts as a barrier in preventing the reverse flow occurring downstream near the the trailing edge from propagating upstream towards the leading edge. This blockade maintains a lower pressure zone upstream of the flap which is otherwise diluted when the reverse flow is allowed to propagate upstream in the absence of the flap. The discontinuity in C_p is more pronounced when the growth and advection of the TEV is prominent in Fig. 10b–10c. During these instances, the TEV strongly induces reverse flow directed from the trailing to the leading edge. For the flap-less case, this aggravated TEV induced reverse flow can be visualized in the vorticity plots in Fig. 3f–3g where streamlines are superimposed on the contours for clarity. In these plots, several upstream propagating streamlines can be observed at t/T = 0.27, 0.55. On the other hand, the presence of the flap significantly reduces those streamlines in Fig. 10f–10g. Therefore, in the flap-shear regime, significant lift improvements are observed due to the pressure dam effect where the flap effectively blocks the TEV induced reverse flow.

The most amount of blocking of the TEV induced reverse flow is achieved when the flap is highly extended towards the shear layer as seen for the above case of $k_{\beta} = 0.0015$. However, as the flap deflection decreases with increasing stiffness, the blockade constructed by the flap reduces which detrimentally allows the upstream propagation of reverse flow. This increase in reverse flow with increasing stiffness is visualized from the vorticity contours for the flap at 50% location, $i_{\beta} = 0.001$ and stiffness of $k_{\beta} = 0.0015$ and $k_{\beta} = 0.002$ plotted at a time instant of t/T = 0.55 in Fig.

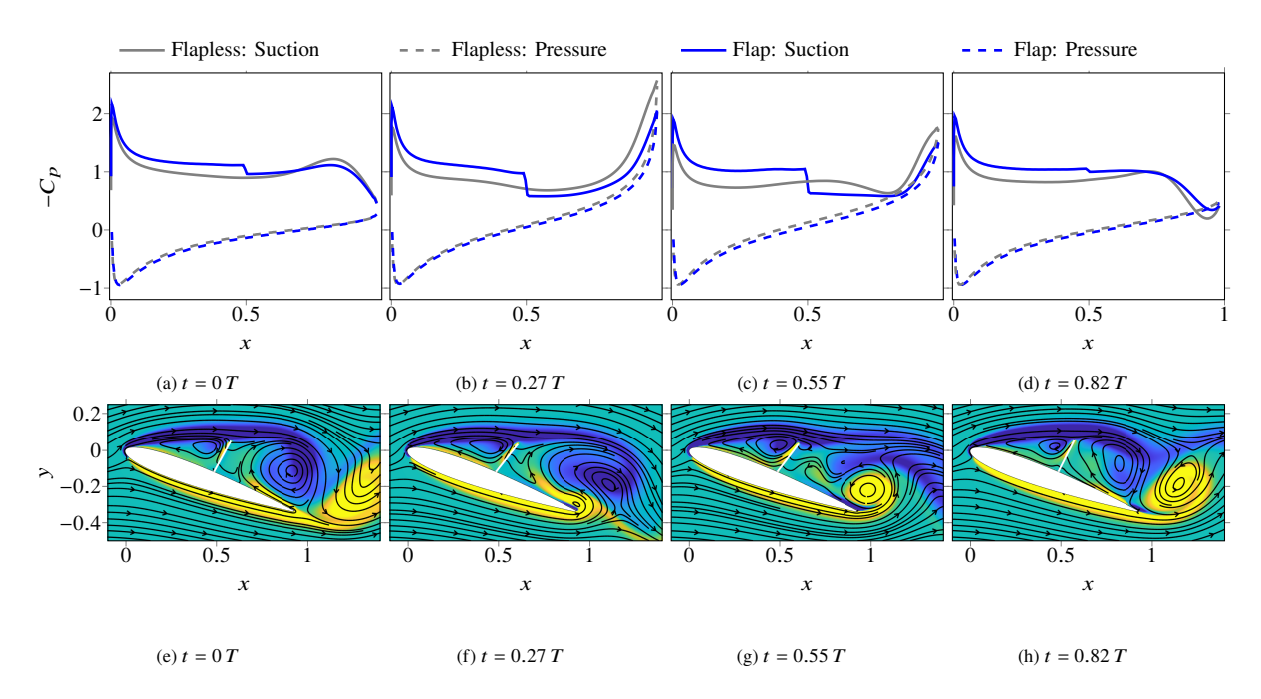


Fig. 10 Comparison of a representative case of $k_{\beta} = 0.0015$, $i_{\beta} = 0.001$ and 50% location in the flap-shear interaction regime with the flap-less airfoil case at four time instants. First row: plots of C_p on the airfoil surface; second row: vorticity contours and superimposed streamlines of the airfoil-flap system.

11a and 11b, respectively. To demonstrate the effect of reverse flow on the strength of the pressure dam effect, the mean C_p distribution on the airfoil surface in one time period is plotted in Fig. 11c for these cases. Clearly, a stronger low pressure region upstream of the flap (therefore a stronger pressure dam effect) for $k_\beta = 0.0015$ as compared to $k_\beta = 0.002$ is observed. Since $k_\beta = 0.0015$ is observed to block the TEV induced reverse flow the most in the flap-shear regime, $k_\beta = 0.0015$ corresponds to an optimal stiffness for the flap at 50% location. Beyond $k_\beta = 0.0015$ the lift decreases monotonously with increasing stiffness.

The flap-shear regime is also observed when the flap is located at 60% chord, around $k_{\beta} \approx 0.0015$ (c.f. Fig. 9). Similar to the 50% case, the flap is significantly deflected towards the shear layer as seen in Fig. 3a–3d. However, unlike the former, the lift does not monotonously decrease with increasing stiffness beyond $k_{\beta} = 0.0015$. Instead a second peak in lift performance at $k_{\beta} \approx 0.01$ –0.015 is observed. Specifically, for the larger inertia cases, an initial drop in lift with increasing stiffness till $k_{\beta} = 0.005$ due to reduced blocking of reverse flow is observed followed by the emergence of the second peak. This second peak corresponds to the flap-vortex regime (c.f. Fig. 9) and is analyzed in the next section.

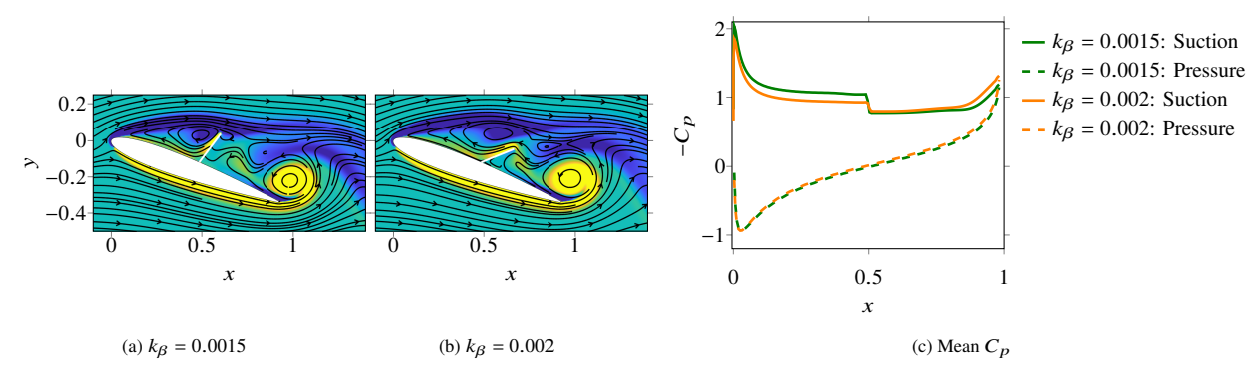


Fig. 11 Demonstration of reduced blocking of TEV induced reverse flow with increasing stiffness via vorticity contour plots at t/T = 0.55 and mean C_p on the airfoil surface for the flap at 50% location and $i_\beta = 0.001$.

E. Flap-vortex interaction regime

We motivate the driving physics in this regime with a representative case of the flap fixed at 60% location, $k_{\beta}=0.01$ and $i_{\beta}=0.001$ and plot C_p on the airfoil surface and corresponding vorticity contours at four time instants in one time period in Fig. 12a–12d and Fig. 12e–12h, respectively. A pressure dam effect similar to the one discerned in the flap-shear interaction regime is observed where an upstream low pressure zone results in a step discontinuity in C_p on the upper surface of the airfoil. However, unlike the flap-shear regime where the flap was largely deployed and solely blocked the TEV induced reverse flow, in the flap-vortex regime, the reduced flap deflection is only able to block this reverse flow during the initial growth of TEV in Fig 12f. As the TEV grows larger in strength, the flap is unable to entirely block the reverse flow as shown in Fig. 12g. However, the reduced flap deflection allows the advection of the LEV through the gap between the flap and the shear layer in Fig. 12g, and this advection process coincides with the growth of the TEV. This downstream advecting, high momentum LEV additionally blocks the TEV induced reverse flow. Altogether, the flap and LEV operate in conjunction to mitigate the propagation of TEV induced reverse flow manifested as reduced number of streamlines propagating from the trailing to the leading edge as compared to the baseline case in Fig. 3e–3h.

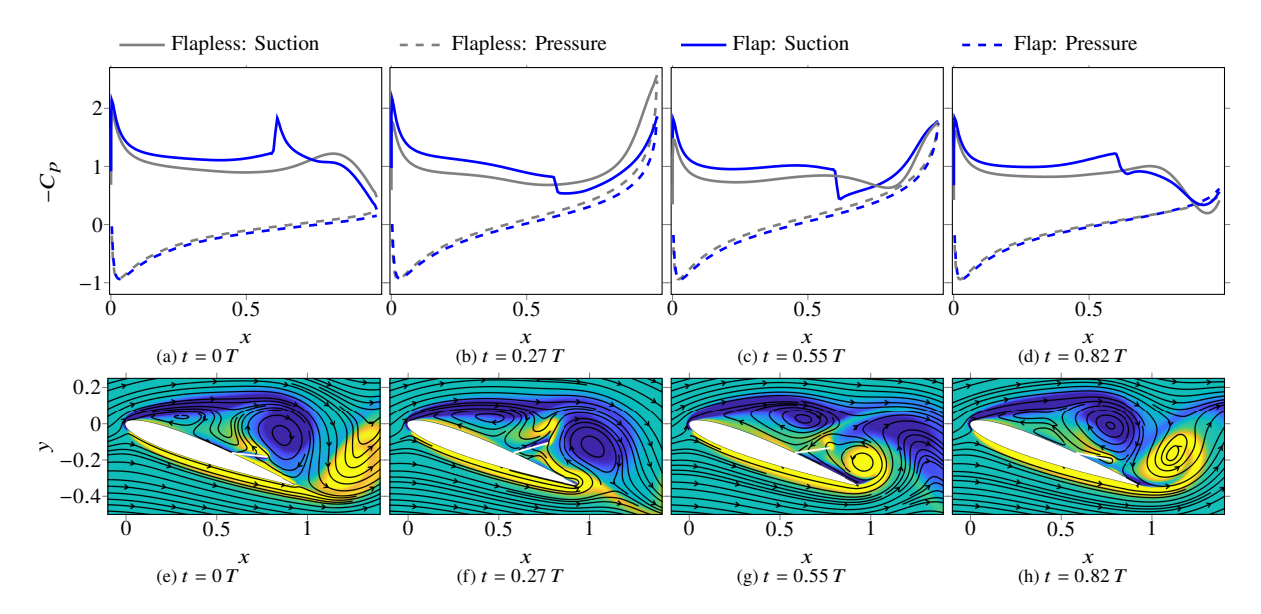


Fig. 12 Comparison of a representative case of $k_{\beta}=0.01$, $i_{\beta}=0.001$ and 60% location in the flap-shear interaction regime with the flap-less airfoil case at four time instants. First row: plots of C_p on the airfoil surface; second row: vorticity contours and superimposed streamlines of the airfoil-flap system.

F. Comparison between flap-shear and flap-vortex interaction regimes

In this section, we compare the characteristics of the flap-shear and flap-vortex regimes by plotting the mean C_p distribution on the airfoil surface for 60% location, $i_\beta=0.001$ and $k_\beta=0.0015$ and $k_\beta=0.01$ in Fig. 13. It can be seen that the main differences between these cases lie in the suction surface C_p . The flap-shear regime case of $k_\beta=0.0015$ has a stronger pressure dam effect (i.e. lower pressure region upstream of the hinge location) as compared to $k_\beta=0.01$ in the flap-vortex regime. This is because the flap in the flap-shear regime blocks the TEV induced reverse flow more as compared to the flap-vortex regime, as the flap is significantly extended towards the shear layer. On the other hand, the flap-vortex regime case of $k_\beta=0.01$ has an advantageous lower suction C_p in the region downstream of the flap, specifically near the trailing edge, as compared to $k_\beta=0.0015$. This is because the significant blocking of reverse flow in the flap-shear regime comes at the cost of the distortion of LEV as it advects above and around the flap as seen from Fig. 10f–10h. On the other hand, in the flap-vortex regime, the reduced flap deflection allows an efficient advection of LEV with minimal distortion as seen from Fig. 12f–12h. Since the reduced flap deflection in the flap-vortex regime maintains a stronger LEV strength whose lift enhancing effect is most prominent near the trailing edge, a stronger suction C_p downstream of the flap hinge is observed.

To summarize, the cases in the flap-shear and flap-vortex regimes relatively contribute more to the lift generated by

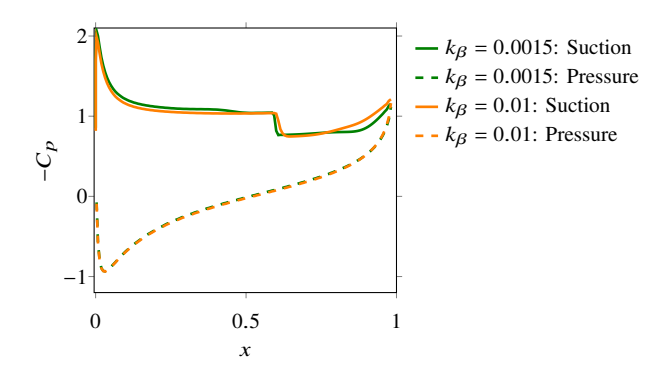


Fig. 13 Comparison between flap-shear and flap-vortex interaction regimes via mean C_p on the airfoil surface for $k_\beta = 0.0015$ and $k_\beta = 0.01$, respectively, with the flap at 60% location and $i_\beta = 0.001$.

the hinge-relative upstream and downstream locations on the suction airfoil surface, respectively, due to the competing effects of blocking of TEV induced reverse flow and LEV distortion.

V. Conclusions

In this manuscript, we performed high-fidelity 2D simulations of flow past a stationary airfoil with a passively deployable torsional flap mounted on the upper surface. The Reynolds number of the flow was Re = 1,000 and the angle of attack was 20° . A systematic parametric study of this flow problem was performed by varying the moment of inertia of the flap, stiffness of the spring and location of the flap hinge. The performance of this airfoil-flap system was analyzed in terms of percentage change in mean lift relative to the baseline airfoil case without a flap. Lift improvements as high as 27% were achieved, thereby showing the potential use of a torsional flap towards the design of bio-inspired aerial vehicles for enhanced maneuverability at high angles of attack.

The parametric study provided numerous insights about the effect of stiffness and inertia on the airfoil-flap system performance. The main role of stiffness was to determine a mean flap deployment angle which in turn sets the flow regimes and associated aerodynamic performance. On the other hand, inertia determined the time-dependent dynamics of the flap about this mean which was found to be either beneficial or detrimental to performance depending on the flow regime set by stiffness. Based on these physical insights, time-averaged flow quantities were used to identify two lift enhancing flow regimes. The flap-shear interaction regime consisted of parametric cases where the flap tip resided in close proximity to the shear layer, whereas the flap-vortex interaction regime consisted of cases where the flap strongly interacted with the vortex shedding process.

Two length scales characteristic to these regimes were defined and used as inputs to a classification algorithm based on k-means clustering. This classification methodology was able to classify all the parametric cases into four clusters, including the indiscernible cases that were hardly classifiable from the parametric study alone. The first two clusters corresponded to the flap-shear and flap-vortex interaction regimes. The third cluster consisted of cases transitioning between the primary two regimes while the fourth cluster consisted of non-interactive, least-lift enhancing cases.

In the flap-shear and flap-vortex interaction regimes, a pressure dam effect due to the blocking of TEV induced reverse was found to be the dominant physical mechanism responsible for delivering significant lift improvements. While in the flap-shear regime, the flap was highly deployed towards the shear layer and significantly blocked the reverse flow, in the flap-vortex regime, the flap as well as the LEV operated in conjunction to achieve a similar blockade. A stronger pre-flap contribution to lift was provided by the flap-shear regime cases since they blocked the reverse flow the most. On the other hand, a stronger post-flap lift contribution was provided by the flap-vortex regime cases since they allowed an efficient advection of LEV with minimal distortion.

VI. Acknowledgements

We gratefully acknowledge funding through the National Science Foundation under grant CBET 20-29028. We also thank Aimy Wissa and Chengfang Duan for the discussions on exploring the flow physics of the airfoil-flap system.

References

- [1] Carruthers, A. C., Thomas, A. L., and Taylor, G. K., "Automatic aeroelastic devices in the wings of a steppe eagle Aquila nipalensis," *Journal of Experimental Biology*, Vol. 210, No. 23, 2007, pp. 4136–4149.
- [2] Videler, J. J., Avian flight, Oxford University Press, 2006.
- [3] Jiakun, H., Zhe, H., Fangbao, T., and Gang, C., "Review on bio-inspired flight systems and bionic aerodynamics," *Chinese Journal of Aeronautics*, 2020.
- [4] Bechert, D., Bruse, M., Hage, W., and Meyer, R., "Fluid mechanics of biological surfaces and their technological application," *Naturwissenschaften*, Vol. 87, No. 4, 2000, pp. 157–171.
- [5] Duan, C., Waite, J., and Wissa, A., "Design optimization of a covert feather-inspired deployable structure for increased lift," 2018 Applied Aerodynamics Conference, 2018, p. 3174.
- [6] Schluter, J. U., "Lift enhancement at low Reynolds numbers using self-activated movable flaps," *Journal of aircraft*, Vol. 47, No. 1, 2010, pp. 348–351.
- [7] Kernstine, K., Moore, C., Cutler, A., and Mittal, R., "Initial Characterization of Self-Activated Movable Flaps," Pop-Up Feathers"," 46th AIAA Aerospace Sciences Meeting and Exhibit, 2008, p. 369.
- [8] Duan, C., and Wissa, A., "Covert-inspired flaps for lift enhancement and stall mitigation," Bioinspiration & Biomimetics, 2021.
- [9] Johnston, J., and Gopalarathnam, A., "Investigation of a bio-inspired lift-enhancing effector on a 2D airfoil," *Bioinspiration & biomimetics*, Vol. 7, No. 3, 2012, p. 036003.
- [10] Bramesfeld, G., and Maughmer, M. D., "Experimental investigation of self-actuating, upper-surface, high-lift-enhancing effectors," *Journal of aircraft*, Vol. 39, No. 1, 2002, pp. 120–124.
- [11] Meyer, R., Hage, W., Bechert, D. W., Schatz, M., Knacke, T., and Thiele, F., "Separation control by self-activated movable flaps," *AIAA journal*, Vol. 45, No. 1, 2007, pp. 191–199.
- [12] Linehan, T., and Mohseni, K., "Scaling trends of bird's alular feathers in connection to leading-edge vortex flow over hand-wing," *Scientific reports*, Vol. 10, No. 1, 2020, pp. 1–14.
- [13] Fang, Z., Gong, C., Revell, A., Chen, G., Harwood, A., and O'Connor, J., "Passive separation control of a NACA0012 airfoil via a flexible flap," *Physics of Fluids*, Vol. 31, No. 10, 2019, p. 101904.
- [14] Rosti, M. E., Omidyeganeh, M., and Pinelli, A., "Passive control of the flow around unsteady aerofoils using a self-activated deployable flap," *Journal of Turbulence*, Vol. 19, No. 3, 2018, pp. 204–228.
- [15] Goza, A., and Colonius, T., "A strongly-coupled immersed-boundary formulation for thin elastic structures," *Journal of Computational Physics*, Vol. 336, 2017, pp. 401–411.
- [16] Nair, N. J., and Goza, A., "A strongly coupled immersed boundary method for fluid-structure interaction that mimics the efficiency of stationary body methods," *arXiv preprint arXiv:2103.06415*, 2021.
- [17] Colonius, T., and Taira, K., "A fast immersed boundary method using a nullspace approach and multi-domain far-field boundary conditions," *Computer Methods in Applied Mechanics and Engineering*, Vol. 197, No. 25-28, 2008, pp. 2131–2146.